BJR


Received: 27 May 2016 | Revised: 16 August 2016 | Accepted: 26 September 2016

http://dx.doi.org/10.1259/bjr.20160480

Cite this article as:
Schyns LEJR, Almeida IP, Van Hoof SJ, Descamps B, Vanhove C, Landry G, et al. Optimizing dual energy cone beam CT protocols for preclinical imaging and radiation research. *Br J Radiol* 2016; **89**: 20160480.

## SMALL ANIMAL IGRT SPECIAL FEATURE: FULL PAPER

# Optimizing dual energy cone beam CT protocols for preclinical imaging and radiation research

**[1]LOTTE E J R SCHYNS, MSc, [1]ISABEL P ALMEIDA, MSc, [1]STEFAN J VAN HOOF, MSc, [2]BENEDICTE DESCAMPS, PhD, [2]CHRISTIAN VANHOVE, PhD, [3]GUILLAUME LANDRY, PhD, [1]PATRICK V GRANTON, PhD and [1,4]FRANK VERHAEGEN, PhD**

[1]Department of Radiation Oncology (MAASTRO), GROW—School for Oncology and Developmental Biology, Maastricht University Medical Centre, Maastricht, Netherlands
[2]iMinds Medical IT–IBiTech–MEDISIP–INFINITY, De Pintelaan 185, Ghent, Belgium
[3]Department of Medical Physics, Faculty of Physics, Ludwig-Maximilians-Universität München (LMU Munich), Munich, Germany
[4]Medical Physics Unit, Department of Oncology, McGill University, Montréal, QC, Canada

Address correspondence to: Prof Dr Frank Verhaegen
E-mail: *frank.verhaegen@maastro.nl*

**Objective:** The aim of this work was to investigate whether quantitative dual-energy CT (DECT) imaging is feasible for small animal irradiators with an integrated cone-beam CT (CBCT) system.
**Methods:** The optimal imaging protocols were determined by analyzing different energy combinations and dose levels. The influence of beam hardening effects and the performance of a beam hardening correction (BHC) were investigated. In addition, two systems from different manufacturers were compared in terms of errors in the extracted effective atomic numbers ($Z_{eff}$) and relative electron densities ($\rho_e$) for phantom inserts with known elemental compositions and relative electron densities.
**Results:** The optimal energy combination was determined to be 50 and 90 kVp. For this combination, $Z_{eff}$ and $\rho_e$ can be extracted with a mean error of 0.11 and 0.010, respectively, at a dose level of 60 cGy.
**Conclusion:** Quantitative DECT imaging is feasible for small animal irradiators with an integrated CBCT system. To obtain the best results, optimizing the imaging protocols is required. Well-separated X-ray spectra and a sufficient dose level should be used to minimize the error and noise for $Z_{eff}$ and $\rho_e$. When no BHC is applied in the image reconstruction, the size of the calibration phantom should match the size of the imaged object to limit the influence of beam hardening effects. No significant differences in $Z_{eff}$ and $\rho_e$ errors are observed between the two systems from different manufacturers.
**Advances in knowledge:** This is the first study that investigates quantitative DECT imaging for small animal irradiators with an integrated CBCT system.

## INTRODUCTION

Dual-energy CT (DECT) imaging is now commonly used for a wide range of radiological purposes and shows potential for improving various parts of the radiotherapy workflow.[1] It has already been shown that DECT imaging can improve the accuracy of tissue segmentation and Monte Carlo dose calculations in the kilovoltage energy range,[2–8] which is promising for small animal radiotherapy. However, for preclinical imaging and small animal radiotherapy purposes, DECT imaging is still largely unexplored. Previous research in the field of small animal DECT imaging focused on using nanoparticle-based contrast agents to investigate atherosclerotic plaques, tumour vasculature and cardiac injury.[9–13]

For DECT imaging, two images are acquired with two different X-ray spectra, which can be obtained by applying different X-ray tube voltages and/or different filters. The resulting CT number images can be decomposed into effective atomic number ($Z_{eff}$) images and relative electron density ($\rho_e$) images.[14,15] The current small animal irradiators with an integrated cone-beam CT (CBCT) system are not able to acquire the two different images simultaneously. However, the images can be acquired consecutively.

To achieve the typical submillimetre voxel sizes in small animal imaging, a relatively high imaging dose is required, which is generally one or two orders of magnitude higher than that in human imaging.[16,17] Although higher dose levels lead to better image quality, the imaging doses should always be as low as reasonably achievable to ensure the welfare of the animal and to avoid compromising the biological processes of interest. Tumour growth can be affected by doses exceeding 1 Gy;[18] so, when two CT images are acquired for DECT imaging, the dose level for each acquisition should be below 50 cGy.

Figure 1. Phantom layout. Numbers 1–12 relate to Table 1.

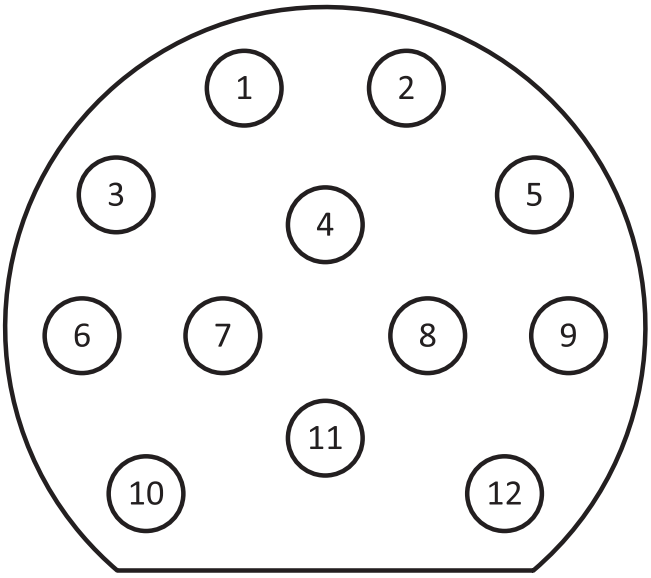


The aim of this work was to investigate whether quantitative DECT imaging is feasible for small animal irradiators with an integrated CBCT system. The optimal imaging protocols were determined by analyzing different energy combinations and dose levels. The influence of beam hardening effects and the performance of a beam hardening correction (BHC) were investigated. In addition, two systems from different manufacturers were compared in terms of errors in the extracted $Z_{eff}$ and $\rho_e$ for phantom inserts with known elemental compositions and relative electron densities.

## METHODS AND MATERIALS

### Mini phantoms

A series of measurements and simulations were performed using two mini phantoms each with 12 cylindrical inserts that have a 3.5-mm diameter (SmART Scientific Solutions, Maastricht, Netherlands). Figure 1 shows the phantom layout and Table 1 lists the $Z_{eff}$ and $\rho_e$ reference values provided by the manufacturer. One phantom, containing parts of tissue-equivalent inserts of a Gammex RMI 467 phantom (Gammex, Middleton, WI), was used for calibration. The other phantom, containing parts of CIRS 002ED inserts (CIRS, Norfolk, VA) plus other materials with known $Z_{eff}$ and $\rho_e$, was used for validation. The water insert was created by filling a nuclear magnetic resonance (NMR) sample tube (Wilmad-LabGlass, Vineland, NJ) with distilled water. The inserts are contained in a Gammex CT Solid Water casing with a 3-cm diameter and a 1-cm width.

### Imaging protocols

For the first set of measurements, the mini phantoms were imaged using an X-RAD 225Cx system (Precision X-ray, North Branford, CT).[19] The images were acquired for a series of X-ray tube voltages ranging from 40 to 100 kV in 10-kV increments. Each of the seven X-ray spectra were filtered with 2 mm of aluminium. The acquired images were reconstructed into a $328 \times 311 \times 591$ matrix with a $103 \times 103 \times 103$-$\mu m^3$ voxel size using a Feldkamp back projection algorithm.[20] To achieve an equivalent dose level of 30 cGy for each energy (60 cGy for any combination of two energies), the exposures (product of tube current and exposure time) listed in Table 2 were used. To verify the dose level for each energy, measurements using a TN30012 Farmer-type ionization chamber (PTW, Freiburg, Germany) were performed according to the AAPM TG-61 protocol for kilovoltage X-ray beam dosimetry to determine the absorbed dose to water at the surface of the phantom.[21] The dose inside the phantom is considerably lower than the surface dose.

For all 21 energy combinations, a separate calibration and validation were performed.

Table 1. Effective atomic number ($Z_{eff}$) and relative electron density ($\rho_e$) reference values provided by the manufacturer

| Calibration phantom | | | | Validation phantom | | | |
|---|---|---|---|---|---|---|---|
| Number | Insert name | $Z_{eff}$ | $\rho_e$ | Number | Insert name | $Z_{eff}$ | $\rho_e$ |
| 1 | Gammex AP6 Adipose | 6.21 | 0.928 | 1 | Gammex BR12 Breast | 6.93 | 0.956 |
| 2 | Gammex CT Solid Water | 7.74 | 0.992 | 2 | Teflon | 8.46 | 1.860 |
| 3 | Gammex IB3 Inner Bone | 10.42 | 1.086 | 3 | Lucite | 6.53 | 1.146 |
| 4 | Gammex SR2 Brain | 6.09 | 1.047 | 4 | Air | 7.71 | 0.001 |
| 5 | Gammex CB2-30% CaCO3 | 10.90 | 1.276 | 5 | PMMA | 6.53 | 1.156 |
| 6 | Gammex BR12 Breast | 6.93 | 0.956 | 6 | Paraffin Wax | 5.48 | 0.959 |
| 7 | Air | 7.71 | 0.001 | 7 | Water | 7.48 | 1.000 |
| 8 | Water | 7.48 | 1.000 | 8 | CIRS Muscle | 7.59 | 1.041 |
| 9 | Gammex B200 Bone Mineral | 10.42 | 1.103 | 9 | Air | 7.71 | 0.001 |
| 10 | Gammex LV1 Liver | 7.74 | 1.064 | 10 | Air | 7.71 | 0.001 |
| 11 | Gammex SB3 Cortical Bone | 13.64 | 1.695 | 11 | CIRS Adipose | 6.44 | 0.956 |
| 12 | Gammex CB2-50% CaCO3 | 12.54 | 1.469 | 12 | CIRS Bone | 11.90 | 1.507 |

Table 2. Exposures for the different X-ray tube voltages

| Tube voltage (kV) | Exposure (mAs) |
|---|---|
| 40 | 1111.2 |
| 50 | 670.8 |
| 60 | 477.0 |
| 70 | 369.6 |
| 80 | 300.0 |
| 90 | 249.6 |
| 100 | 213.6 |

To investigate the influence of the dose level on the mean error and standard deviation for $Z_{eff}$ and $\rho_e$, the total dose level of 60 cGy for the optimal energy combination was reduced to 45 and 30 cGy. New images were acquired using the X-RAD 225Cx system and a new calibration and validation were performed for each dose level.

The influence of beam hardening effects was investigated by performing simulations using ImaSim.[22] Seven different X-ray spectra, equivalent to the ones used for the measurements, were generated with SpekCalc.[23–25] These spectra were used to simulate images of both the calibration and validation phantom with different diameters of 3, 5 and 7 cm, as shown in Figure 2. The image reconstruction was performed with and without ImaSim's built-in BHC, which is based on water attenuation properties. Assuming that the imaged object is cylindrical and made of water, an ideal projection is calculated as the weighted sum over the real projection and the linear attenuation coefficient of water which is a function of the X-ray spectrum and path length through the cylinder. As a final step, the back projection is performed using the ideal projections instead of the real projections.

The accuracy of the simulations was evaluated by comparing the $Z_{eff}$ and $\rho_e$ values that were extracted from the ImaSim simulations to the $Z_{eff}$ and $\rho_e$ values that were extracted from the X-RAD 225Cx acquisitions. A good correspondence was found; the mean difference between the simulated and measured values equals 1.5% for $Z_{eff}$ and 1.0% for $\rho_e$ (Appendix A) (Figure A1).

The results for the X-RAD 225Cx system were compared with the small animal radiation research platform (SARRP) (Xstrahl, Camberley, UK).[26] Also for the SARRP, images of both mini phantoms were acquired for a series of X-ray tube voltages ranging from 40 to 100 kV in 10-kV increments. Each of the seven X-ray spectra were filtered with 1 mm of aluminium. The acquired images were reconstructed into a $512 \times 512 \times 512$ matrix with a $103 \times 103 \times 103$-$\mu m^3$ voxel size using a Feldkamp back projection algorithm.[20] For both systems, the same exposures (listed in Table 2) were used, which leads to a higher dose level for the SARRP (1-mm aluminium filtration; 43 cGy for each energy) than that for the X-RAD 225Cx system (2-mm aluminium filtration; 30 cGy for each energy). The slices were acquired in the radial direction of the phantoms; so, for the

Figure 2. Simulated CT images (50 kVp) of the phantoms with different diameters: 3, 5 and 7 cm (top row: calibration phantom, bottom row: validation phantom).

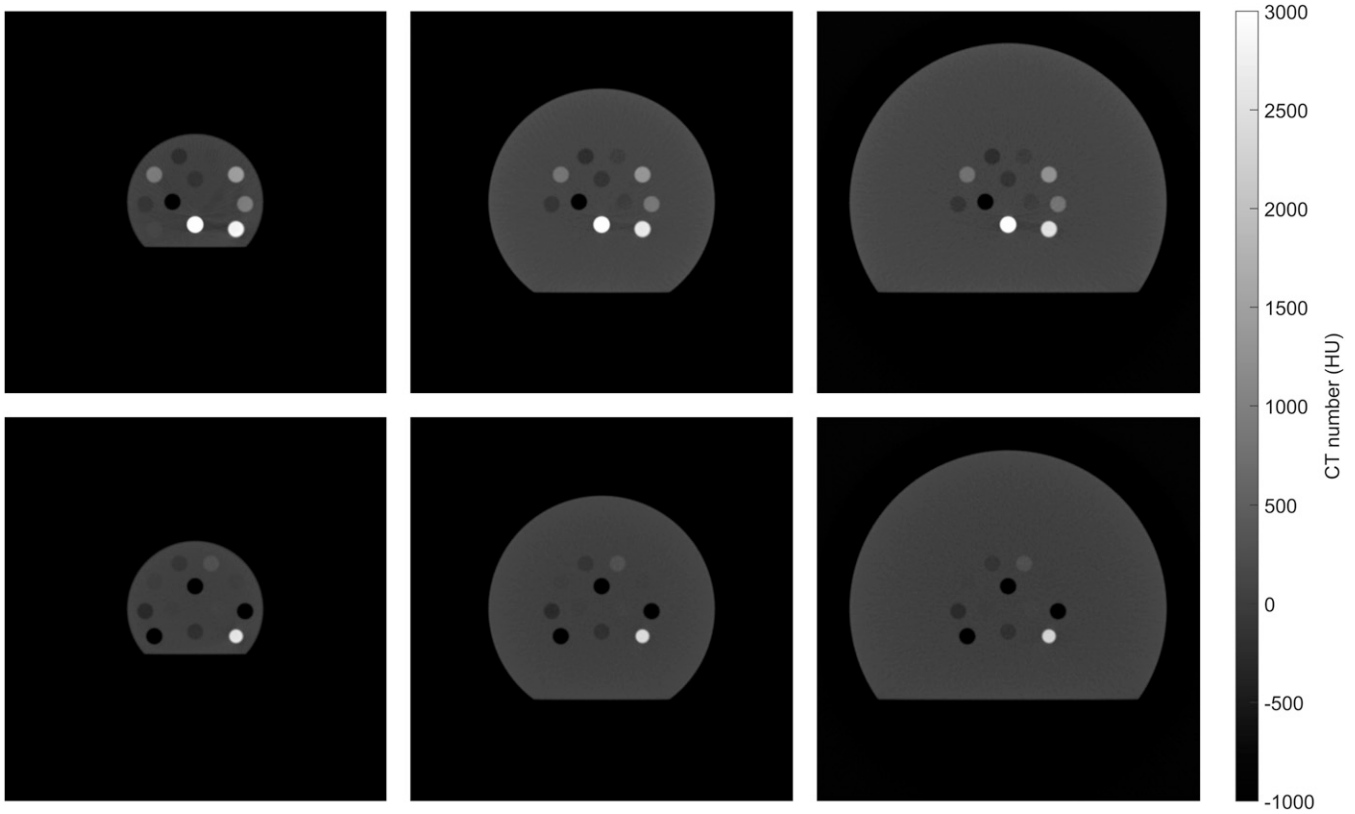

X-RAD 225Cx system with the rotating gantry and fixed table, the phantom's cylindrical axis was positioned horizontally. For the SARRP with the rotating table, the phantom's cylindrical axis was positioned vertically.

### Extracting the effective atomic number and relative electron density

$Z_{eff}$ was extracted using the tissue substitute method described by Landry et al,[14] which is based on a parameterization of the ratio of high- and low-energy linear attenuation coefficients. The ratio is defined as $\mu_{ratio}=\frac{\mu_{LowEnergy}}{\mu_{HighEnergy}}$ and is calculated for each individual voxel. The mean $\mu_{ratio}$ for each insert was calculated in a circular region of interest in the four central slices of the calibration phantom. The mean $\mu_{ratio}$ for the different inserts was plotted as a function of the reference $Z_{eff}$. The following calibration curve was fitted through these points. In this equation, both $\mu_{LowEnergy}$ and $\mu_{HighEnergy}$ are relative to the linear attenuation coefficient of water and $A$, $B$, $C$, $D$, $E$, $F$, $n$ and $m$ are fit parameters.

$$\mu_{ratio}=\frac{\mu_{LowEnergy}}{\mu_{HighEnergy}}=\frac{A+B\cdot {Z_{eff}}^{n-1}+C\cdot {Z_{eff}}^{m-1}}{D+E\cdot {Z_{eff}}^{n-1}+F\cdot {Z_{eff}}^{m-1}}$$

For the validation, $Z_{eff}$ was solved separately for each voxel by calculating $\mu_{ratio}$ from the corresponding voxels in the images that were acquired with the low- and high-energy X-ray spectra. The mean $Z_{eff}$ for each insert was calculated in a circular region of interest in the four central slices of the validation phantom and then compared with the reference value that is provided by the manufacturer.

It is not possible to solve for $Z_{eff}$ when $\mu_{ratio}$ is below the minimum of the calibration curve. For example, in the case of the 50- and 90-kVp combination, which is shown in Figure 3, the minimum $\mu_{ratio}$ is indicated by the dashed line and equals approximately 0.68.

All voxels to which no $Z_{eff}$ value could be assigned were excluded from the analysis (generally <0.01% of the voxels in the regions of interest). Most of the excluded voxels are located at sharp transitions between air and the solid water casing. This might be caused by partial volume effects; air and solid water both partially fill the voxel and are combined into a voxel with a CT number that corresponds to neither air nor solid water.

$\rho_e$ was extracted using a method described by Saito et al,[15] which is based on a single linear relationship between a weighted subtraction of CT numbers and $\rho_e$. The weighted subtraction of CT numbers is defined as $\Delta HU=(1+\alpha)\cdot HU_{HighEnergy}-\alpha\cdot HU_{LowEnergy}$, in which $\alpha$ is the weighting factor. The mean $HU_{LowEnergy}$ and $HU_{HighEnergy}$ for each insert were calculated in a circular region of interest in the four central slices of the calibration phantom. The reference $\rho_e$ was plotted as a function of the mean $HU_{LowEnergy}$ and $HU_{HighEnergy}$ for the different inserts. The following calibration curve was fitted through these points. In this equation, $a$, $b$ and $\alpha$ are fit parameters.

$$\rho_e=a\cdot\frac{(1+\alpha)\cdot HU_{HighEnergy}-\alpha\cdot HU_{LowEnergy}}{1000}+b$$

For the validation, $\rho_e$ was solved separately for each voxel by calculating ΔHU from the corresponding voxels in the images that were acquired with the low- and high-energy X-ray spectra. The mean $\rho_e$ for each insert was calculated in a circular region of interest in the four central slices of the validation phantom and then compared with the reference value that is provided by the manufacturer.

## RESULTS

### Optimal energy combination

The mean $Z_{eff}$ and $\rho_e$ error for different energy combinations (X-RAD 225Cx) are shown in Figure 4. The largest errors were

Figure 3. Effective atomic number ($Z_{eff}$) – $\mu_{ratio}$ calibration curve [50- and 90-kVp combination; X-RAD 225Cx (Precision X-ray, North Branford, CT)]. The dashed line indicates the minimum $\mu_{ratio}$ for which a $Z_{eff}$ value can be assigned.

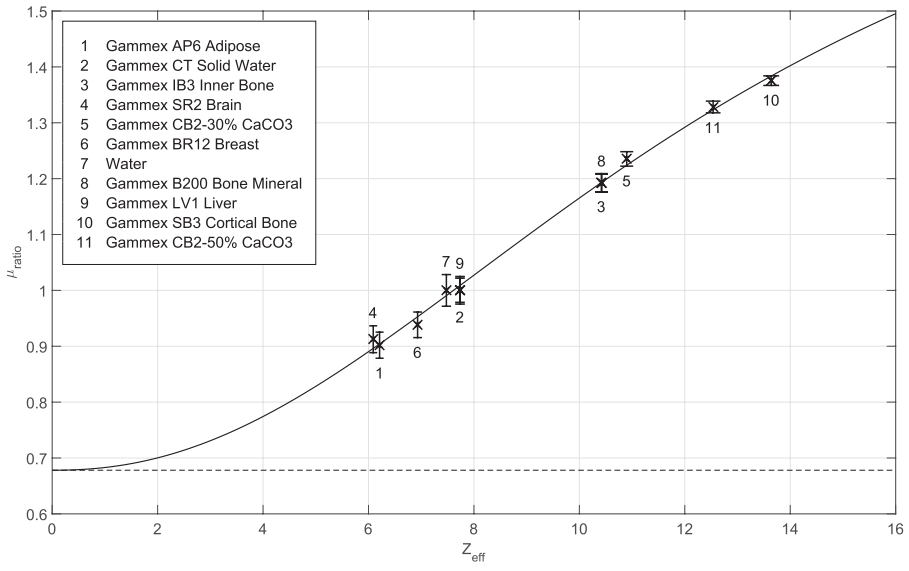

Figure 4. Mean effective atomic number ($Z_{eff}$) and relative electron density ($\rho_e$) error for different energy combinations [X-RAD 225Cx (Precision X-ray, North Branford, CT)].

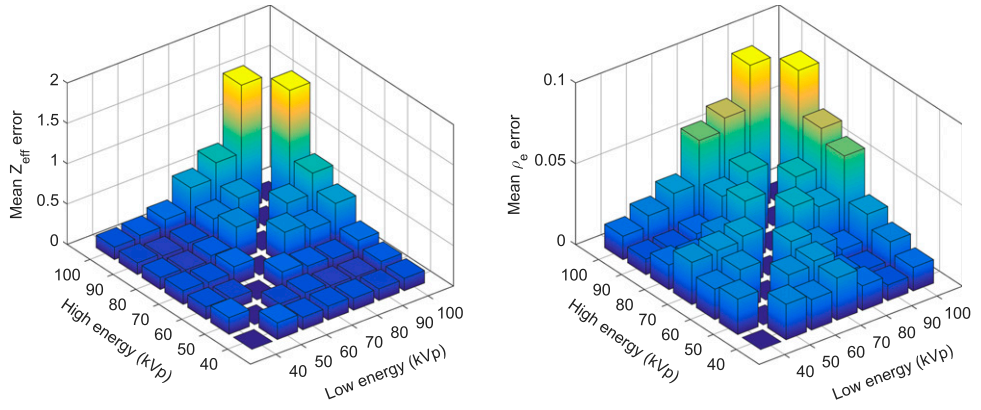


found close to the diagonal, *i.e.* for similar X-ray tube voltages. This can be explained by the fact that these X-ray spectra have a large spectral overlap, meaning that the image acquired with the second spectrum does not add much information. Combinations with the 100-kVp spectrum also showed inferior results. With this exception, all combinations with well-separated X-ray spectra (≥20-kVp difference) produced acceptable results with a mean $Z_{eff}$ error ≤0.33 and a mean $\rho_e$ error ≤0.030. The smallest errors were obtained for the 50- and 90-kVp combination. For this combination, $Z_{eff}$ and $\rho_e$ can be extracted with a mean error of 0.11 and 0.010, respectively. The relative errors are 1.6% for $Z_{eff}$ and 0.8% for $\rho_e$. The maximum $Z_{eff}$ insert error was obtained for the paraffin wax insert and equals 0.25. The maximum $\rho_e$ insert error was obtained for the polymethyl methacrylate (PMMA) insert and equals 0.034. The errors for each individual insert are shown in Figure 8 (to be discussed below) and the fit parameters are shown in Appendix C (Table A1).

## Different dose levels

Figure 5 shows the mean error and standard deviation for $Z_{eff}$ and $\rho_e$ for different dose levels (50- and 90-kVp combination, X-RAD 225Cx). A decrease in dose leads to an increase in both the error and the standard deviation in quantitative DECT imaging. For the lower dose levels, less photons at the level of the source result in less photons at the level of the imaging panel. This generates a lower signal, which leads to relatively more noise. The results show that this noise also propagates into $Z_{eff}$ and $\rho_e$.

## Beam hardening effects

The mean $Z_{eff}$ and $\rho_e$ errors for the different phantom sizes (50- and 90-kVp combination, ImaSim simulations, no BHC applied) are shown in Figure 6. The smallest errors were found close to the diagonal, *i.e.* for matching sizes of the calibration phantom and validation phantom. The larger errors for the different (non-matching) phantom sizes are caused by beam

Figure 5. Mean error and standard deviation for effective atomic number ($Z_{eff}$) and relative electron density ($\rho_e$) for different dose levels [50- and 90-kVp combination; X-RAD 225Cx (Precision X-ray, North Branford, CT)].

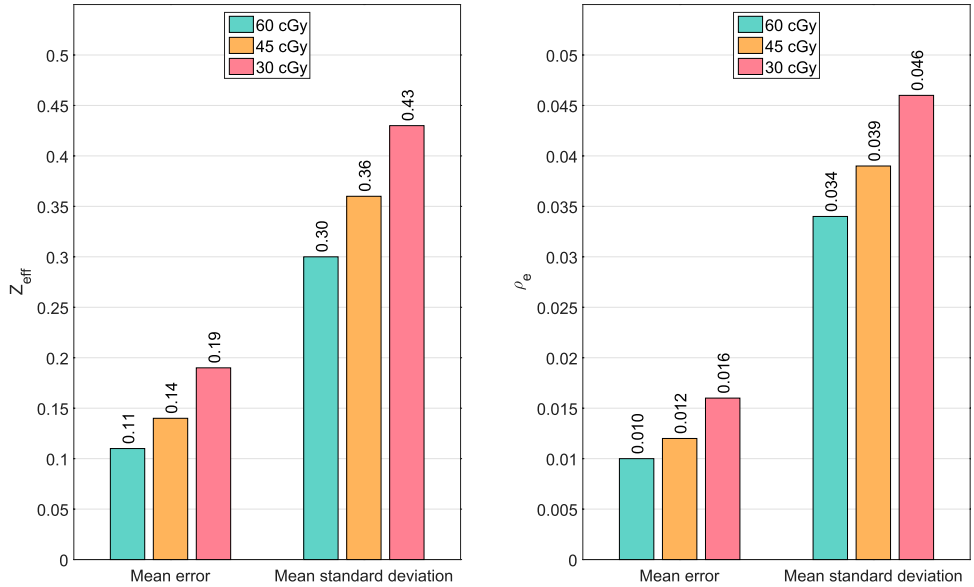

Figure 6. Mean effective atomic number ($Z_{eff}$) and relative electron density ($\rho_e$) error for the different phantom sizes [50- and 90- kVp combination, ImaSim simulations, no beam hardening correction (BHC) applied].

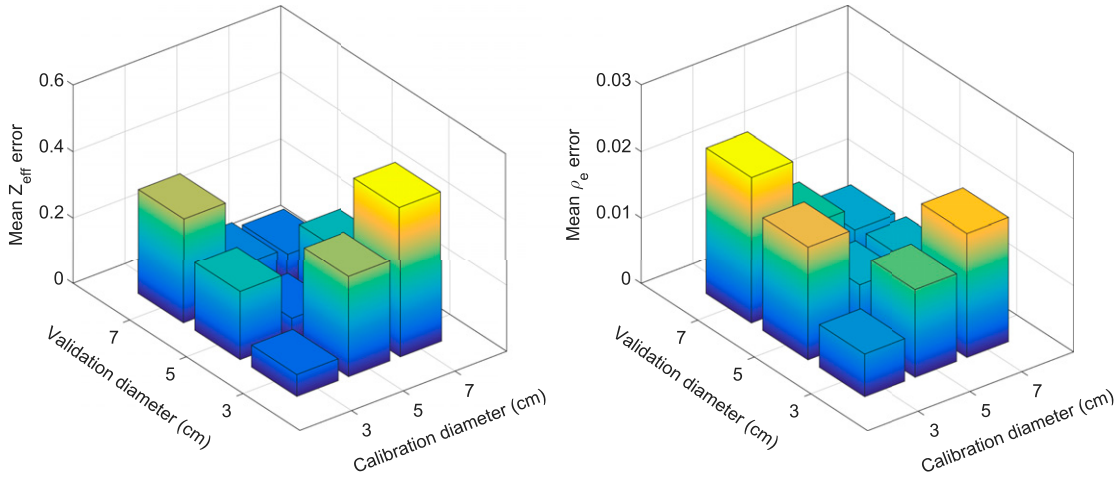


hardening effects; a thicker object increases the mean energy of the X-ray spectra by filtering out the low-energy photons. This change in mean energy is not accounted for in the calibration when the calibration is performed with a phantom that has a different size. The mean $Z_{eff}$ and $\rho_e$ errors are not symmetric with respect to the diagonal, meaning that the errors for the 3-cm calibration combined with the 7-cm validation are different than the errors for the 7-cm calibration combined with the 3-cm validation.

## Beam hardening correction

Figure 7 shows the simulated $Z_{eff}$ and $\rho_e$ with and without BHC (50- and 90-kVp combination, ImaSim simulations). The simulations were performed for one of the worst cases, in which the calibration phantom has a diameter of 3 cm and the validation phantom has a diameter of 7 cm. This is equivalent to performing a quantitative DECT analysis on a rat with a 7-cm diameter when the calibration was performed using the phantom with the 3-cm diameter. Without

Figure 7. Simulated effective atomic number ($Z_{eff}$) and relative electron density ($\rho_e$) with and without beam hardening correction (50- and 90-kVp combination; ImaSim simulations).

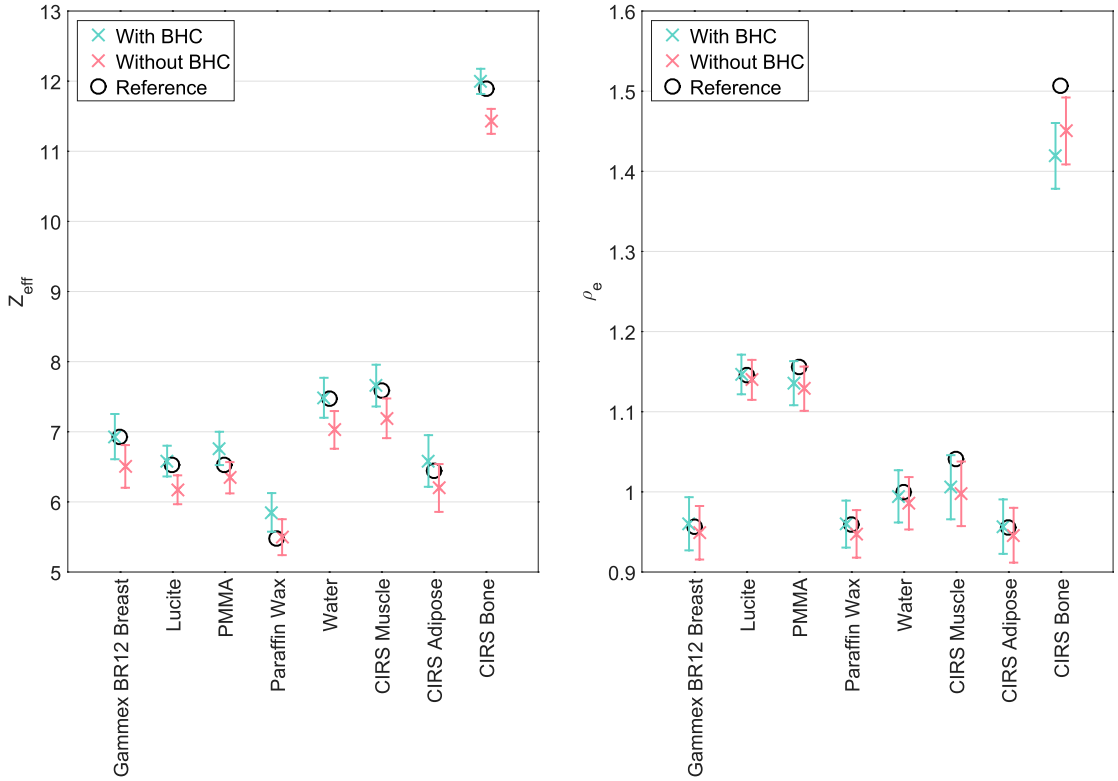

Figure 8. Measured vs reference effective atomic number ($Z_{eff}$) and relative electron density ($\rho_e$) (50- and 90-kVp combination).

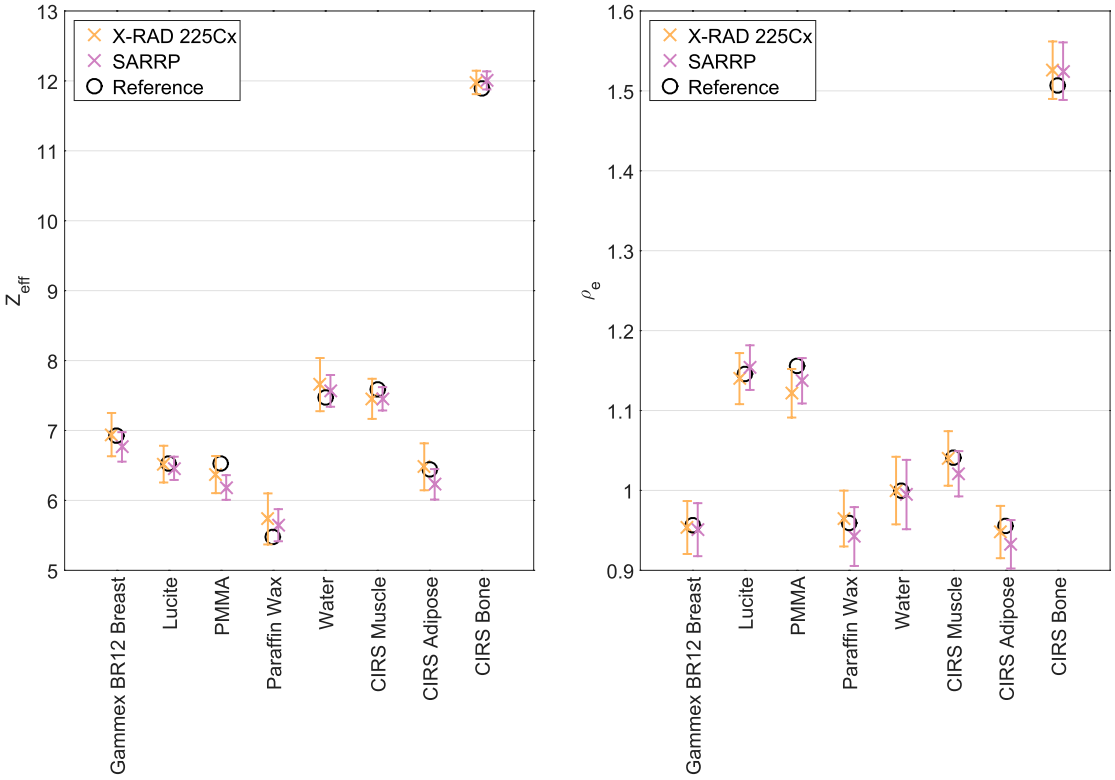


BHC, $Z_{eff}$ and $\rho_e$ can be extracted with a mean error of 0.32 and 0.022, respectively. When applying a BHC in the image reconstruction, $Z_{eff}$ and $\rho_e$ can be extracted with a mean error of 0.12 and 0.019, respectively. Especially for $Z_{eff}$ this is a large increase in accuracy, but also for $\rho_e$ there is a slight increase in accuracy. The relatively large $\rho_e$ error for the CIRS Bone insert can be explained by the fact that the BHC is based on water attenuation properties, which are more appropriate for soft tissues than for bone tissues.

### X-RAD 225Cx *vs* small animal radiation research platform

The optimal energy combination of 50- and 90-kVp for the X-RAD 225Cx system was also determined to be the optimal energy combination for the SARRP. In Figure 8, the measured $Z_{eff}$ and $\rho_e$ for the two systems are compared. Both systems produced values close to the reference values. For the SARRP, $Z_{eff}$ and $\rho_e$ can be extracted with a mean error of 0.16 and 0.014, respectively. The relative errors are 2.4% for $Z_{eff}$ and 1.3% for $\rho_e$. The maximum $Z_{eff}$ insert error was obtained for the PMMA insert and equals 0.34. The maximum $\rho_e$ insert error was obtained for the CIRS Adipose insert and equals 0.023. The X-RAD 225Cx system produced slightly smaller mean errors than the SARRP. A Wilcoxon signed-rank test showed that there are no significant differences in $Z_{eff}$ ($p = 0.313$) and $\rho_e$ ($p = 0.195$) errors between the two systems. However, it should be stated that a higher dose level was used for the SARRP (approximately 86 cGy; 43 cGy for each energy) than for the X-RAD 225Cx system (approximately 60 cGy; 30 cGy for each energy). Examples of CT, $Z_{eff}$ and $\rho_e$ images for both systems are included in Appendix B (Figure A2).

## DISCUSSION

This work shows that $Z_{eff}$ and $\rho_e$ can be extracted with a mean error of 0.11 and 0.010, respectively. Such a high level of accuracy can be obtained only when the two images that are acquired with two different X-ray spectra overlap perfectly geometrically. A small misregistration between the images can cause two non-corresponding voxels to be combined in the analysis, leading to an incorrect $\mu_{ratio}$ and $\Delta$HU, which in turn yields incorrect values for $Z_{eff}$ and $\rho_e$. Therefore, breathing motion might cause a decrease in the accuracy of quantitative DECT imaging. A potential solution to this problem could be the implementation of respiratory gating, *i.e.* excluding projections for a certain breathing phase from the image reconstruction. Another option is to implement fast kilovoltage switching to obtain very short intervals of projections with different X-ray spectra. Separate image reconstructions are then performed for the projections that are acquired with the low- and high-energy spectra.

In the simulations, beam hardening influenced the accuracy of the extracted $Z_{eff}$ and $\rho_e$ values. The best results are obtained when the size of the calibration phantom matches the size of the imaged object. This leads to the conclusion that for the imaging of larger animals, such as rats or rabbits, a larger calibration

phantom is required. To limit the contribution of beam hardening effects, a circular phantom in which the X-rays travel through the same amount of material for each projection is preferred. The X-RAD 225Cx system with the rotating gantry and fixed table acquires slices in the transverse plane of the mouse; so, the X-rays travel through the same amount of material for each projection. The SARRP with the rotating table acquires slices in the coronal plane. For some angles, the X-rays travel through the long (craniocaudal) axis of the animal and for other angles, the X-rays travel through the short (lateral) axis of the animal. This implies that for the SARRP, a decrease in the accuracy of quantitative DECT imaging can be expected for animals and other non-circular objects. Applying a BHC in the image reconstruction showed to increase the accuracy of the extracted $Z_{eff}$ and $\rho_e$ values. At the moment, however, neither the X-RAD 225Cx system nor the SARRP have a BHC implemented in their image reconstruction software.

To achieve a high accuracy in tissue segmentation and Monte Carlo dose calculations, it is important to reduce $Z_{eff}$ and $\rho_e$ errors. Quantitative DECT imaging can be further optimized by, for *e.g.*, applying different levels of filtration to the low- and high-energy X-ray spectra to improve the spectral separation. Simulation models are a useful tool to explore different kinds of optimization possibilities.

## CONCLUSION

It can be concluded that quantitative DECT imaging is feasible for small animal irradiators with an integrated CBCT system. To obtain the best results, optimization of the imaging protocols is required. Well-separated X-ray spectra (≥20-kVp difference) and a sufficient dose level (approximately 60 cGy; 30 cGy for each energy) should be used to minimize the error and noise for $Z_{eff}$ and $\rho_e$. When no BHC is applied in the image reconstruction, the size of the calibration phantom should match the size of the imaged object to limit the influence of beam hardening effects. No significant differences in $Z_{eff}$ and $\rho_e$ errors are observed between the X-RAD 225Cx system and the SARRP.

## ACKNOWLEDGMENTS

The authors would like to thank Gammex (Middleton, WI) and CIRS (Norfolk, VA) for providing the elemental compositions of the phantom inserts.

## CONFLICTS OF INTEREST

FV, PG and SvH are the founders of SmART Scientific Solutions (Maastricht, Netherlands). In addition, FV, PG and SvH declare that they have received research funding from Precision X-ray (North Branford, CT) and have commercial interests with this company.

## REFERENCES

1. van Elmpt W, Landry G, Das M, Verhaegen F. Dual energy CT in radiotherapy: current applications and future outlook. *Radiother Oncol* 2016; **119**: 137–44. doi: http://dx.doi.org/10.1016/j.radonc.2016.02.026
2. Bazalova M, Carrier JF, Beaulieu L, Verhaegen F. Tissue segmentation in Monte Carlo treatment planning: a simulation study using dual-energy CT images. *Radiother Oncol* 2008; **86**: 93–8. doi: http://dx.doi.org/10.1016/j.radonc.2007.11.008
3. Bazalova M, Carrier JF, Beaulieu L, Verhaegen F. Dual-energy CT-based material extraction for tissue segmentation in Monte Carlo dose calculations. *Phys Med Biol* 2008; **53**: 2439–56. doi: http://dx.doi.org/10.1088/0031-9155/53/9/015
4. Landry G, Reniers B, Murrer L, Lutgens L, Gurp EB, Pignol JP, et al. Sensitivity of low energy brachytherapy Monte Carlo dose calculations to uncertainties in human tissue composition. *Med Phys* 2010; **37**: 5188–98. doi: http://dx.doi.org/10.1118/1.3477161
5. Bazalova M, Graves EE. The importance of tissue segmentation for dose calculations for kilovoltage radiation therapy. *Med Phys* 2011; **38**: 3039–49. doi: http://dx.doi.org/10.1118/1.3589138
6. Landry G, Granton PV, Reniers B, Ollers MC, Beaulieu L, Wildberger JE, et al. Simulation study on potential accuracy gains from dual energy CT tissue segmentation for low-energy brachytherapy Monte Carlo dose calculations. *Phys Med Biol* 2011; **56**: 6257–78. doi: http://dx.doi.org/10.1088/0031-9155/56/19/007
7. Landry G, Reniers B, Granton PV, van Rooijen B, Beaulieu L, Wildberger JE, et al. Extracting atomic numbers and electron densities from a dual source dual energy CT scanner: experiments and a simulation model. *Radiother Oncol* 2011; **100**: 375–9. doi: http://dx.doi.org/10.1016/j.radonc.2011.08.029
8. Côté N, Bedwani S, Carrier JF. Improved tissue assignment using dual-energy computed tomography in low-dose rate prostate brachytherapy for Monte Carlo dose calculation. *Med Phys* 2016; **43**: 2611. doi: http://dx.doi.org/10.1118/1.4947486
9. Bhavane R, Badea C, Ghaghada KB, Clark D, Vela D, Moturu A, et al. Dual-energy computed tomography imaging of atherosclerotic plaques in a mouse model using a liposomal-iodine nanoparticle contrast agent. *Circ Cardiovasc Imaging* 2013; **6**: 285–94. doi: http://dx.doi.org/10.1161/CIRCIMAGING.112.000119
10. Clark DP, Ghaghada K, Moding EJ, Kirsch DG, Badea CT. *In vivo* characterization of tumor vasculature using iodine and gold nanoparticles and dual energy micro-CT. *Phys Med Biol* 2013; **58**: 1683–704. doi: http://dx.doi.org/10.1088/0031-9155/58/6/1683
11. Moding EJ, Clark DP, Qi Y, Li Y, Ma Y, Ghaghada K, et al. Dual-energy micro-computed tomography imaging of radiation-induced vascular changes in primary mouse sarcomas. *Int J Radiat Oncol Biol Phys* 2013; **85**: 1353–9. doi: http://dx.doi.org/10.1016/j.ijrobp.2012.09.027
12. Ashton JR, Clark DP, Moding EJ, Ghaghada K, Kirsch DG, West JL, et al. Dual-energy micro-CT functional imaging of primary lung cancer in mice using gold and iodine nanoparticle contrast agents: a validation study. *PLoS One* 2014; **9**: e88129. doi: http://dx.doi.org/10.1371/journal.pone.0088129
13. Lee CL, Min H, Befera N, Clark D, Qi Y, Das S, et al. Assessing cardiac injury in mice with dual energy-microCT, 4D-microCT, and microSPECT imaging after partial heart irradiation. *Int J Radiat Oncol Biol Phys* 2014;

**88**: 686–93. doi: http://dx.doi.org/10.1016/j.ijrobp.2013.11.238
14. Landry G, Seco J, Gaudreault M, Verhaegen F. Deriving effective atomic numbers from DECT based on a parameterization of the ratio of high and low linear attenuation coefficients. *Phys Med Biol* 2013; **58**: 6851–66. doi: http://dx.doi.org/10.1088/0031-9155/58/19/6851
15. Saito M. Potential of dual-energy subtraction for converting CT numbers to electron density based on a single linear relationship. *Med Phys* 2012; **39**: 2021–30. doi: http://dx.doi.org/10.1118/1.3694111
16. Ford NL, Thornton MM, Holdsworth DW. Fundamental image quality limits for microcomputed tomography in small animals. *Med Phys* 2003; **30**: 2869–77. doi: http://dx.doi.org/10.1118/1.1617353
17. Verhaegen F, Granton P, Tryggestad E. Small animal radiotherapy research platforms. *Phys Med Biol* 2011; **56**: R55–83. doi: http://dx.doi.org/10.1088/0031-9155/56/12/R01
18. Workman P, Aboagye EO, Balkwill F, Balmain A, Bruder G, Chaplin DJ, et al. Guidelines for the welfare and use of animals in cancer research. *Br J Cancer* 2010; **102**: 1555–77. doi: http://dx.doi.org/10.1038/sj.bjc.6605642
19. Clarkson R, Lindsay PE, Ansell S, Wilson G, Jelveh S, Hill RP, et al. Characterization of image quality and image-guidance performance of a preclinical microirradiator. *Med Phys* 2011; **38**: 845–56. doi: http://dx.doi.org/10.1118/1.3533947
20. Feldkamp LA, Davis LC, Kress JW. Practical cone-beam algorithm. *J Opt Soc Am A* 1984; **1**: 612–9. doi: http://dx.doi.org/10.1364/JOSAA.1.000612
21. Ma CM, Coffey CW, DeWerd LA, Liu C, Nath R, Seltzer SM, et al. AAPM protocol for 40–300 kV X-ray beam dosimetry in radiotherapy and radiobiology. *Med Phys* 2001; **28**: 868–93. doi: http://dx.doi.org/10.1118/1.1374247
22. Landry G, deBlois F, Verhaegen F. ImaSim, a software tool for basic education of medical X-ray imaging in radiotherapy and radiology. *Front Phys* 2013. doi: http://dx.doi.org/10.3389/fphy.2013.00022
23. Poludniowski G, Landry G, DeBlois F, Evans PM, Verhaegen F. SpekCalc: a program to calculate photon spectra from tungsten anode x-ray tubes. *Phys Med Biol* 2009; **54**: N433–8. doi: http://dx.doi.org/10.1088/0031-9155/54/19/N01
24. Poludniowski GG, Evans PM. Calculation of X-ray spectra emerging from an X-ray tube. Part I. electron penetration characteristics in X-ray targets. *Med Phys* 2007; **34**: 2164–74. doi: http://dx.doi.org/10.1118/1.2734725
25. Poludniowski GG. Calculation of X-ray spectra emerging from an X-ray tube. Part II. X-ray production and filtration in X-ray targets. *Med Phys* 2007; **34**: 2175–86. doi: http://dx.doi.org/10.1118/1.2734726
26. Wong J, Armour E, Kazanzides P, Iordachita I, Tryggestad E, Deng H, et al. High-resolution, small animal radiation research platform with X-ray tomographic guidance capabilities. *Int J Radiat Oncol Biol Phys* 2008; **71**: 1591–9. doi: http://dx.doi.org/10.1016/j.ijrobp.2008.04.025

## APPENDIX A

In Figure A1, the $Z_{eff}$ and $\rho_e$ values that were extracted from the ImaSim simulations are compared with the $Z_{eff}$ and $\rho_e$ values that were extracted from the X-RAD 225Cx acquisitions. The simulations and measurements were performed for the 50- and 90-kVp combination at a total dose level of 60 cGy. No BHC was applied in the image reconstruction. The calibration and validation were performed separately for the simulations and measurements using the phantoms with a 3-cm diameter. The mean difference between the simulated and measured values equals 1.5% for $Z_{eff}$ and 1.0% for $\rho_e$.

Figure A1. Simulated *vs* measured $Z_{eff}$ and $\rho_e$ (50- and 90-kVp combination).

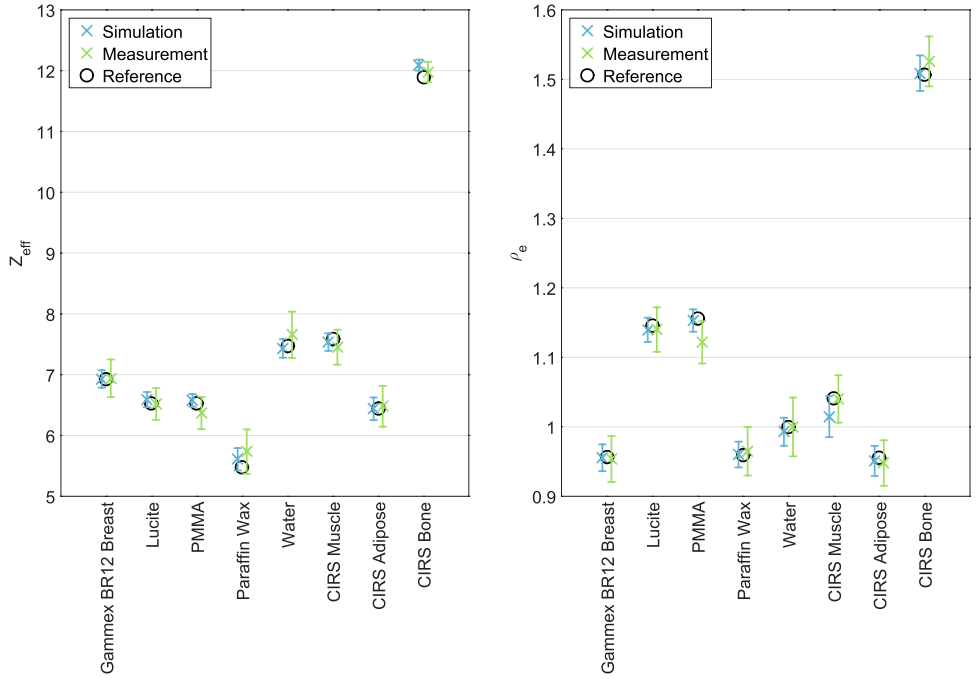

Figure A2. CT, $Z_{eff}$ and $\rho_e$ images of the validation phantom (50- and 90-kVp combination) (top row: X-RAD 225Cx, bottom row: SARRP).

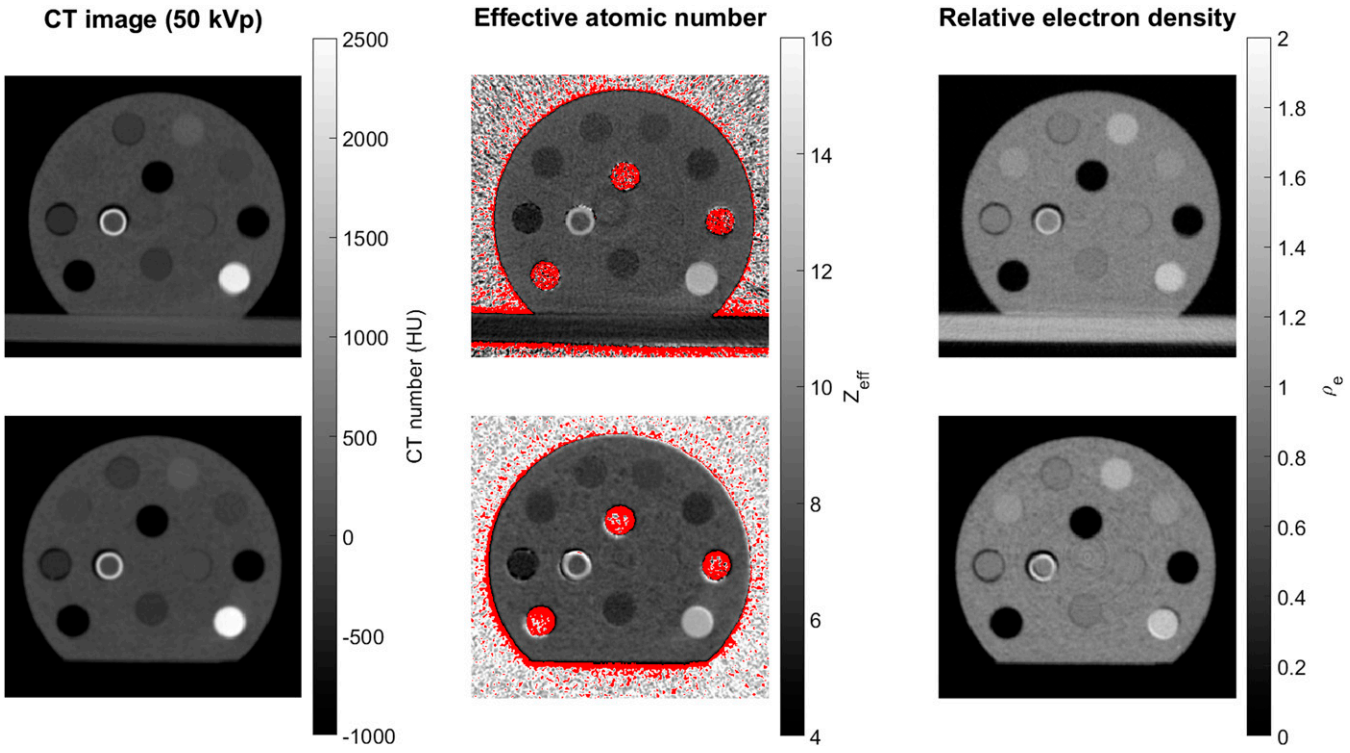


## APPENDIX B

Examples of CT, $Z_{eff}$ and $\rho_e$ images for both systems are shown in Figure A2. The images in the top row were acquired using the X-RAD 225Cx system and the images in the bottom row were acquired using the SARRP. For both systems, the $Z_{eff}$ and $\rho_e$ images were acquired using the 50- and 90-kVp combination. All voxels to which no $Z_{eff}$ value could be assigned are marked with a red colour. The three circular red areas contain air.

## APPENDIX C

Table A1 shows the fit parameters for the $Z_{eff} - \mu_{ratio}$ calibration ($A - F$, $n$, $m$) and $\rho_e - \Delta$HU calibration ($a$, $b$, $\alpha$). The fit parameters for the optimal energy combination of 50 and 90 kVp are listed together with the minimum and maximum values that were found for the 21 energy combinations (X-RAD 225Cx).

Table A1. Fit parameters for the $Z_{eff} - \mu_{ratio}$ calibration ($A - F$, $n$, $m$) and $\rho_e - \Delta$HU calibration ($a$, $b$, $\alpha$)

| Parameter | 50 and 90 kVp | Minimum value | Maximum value |
|---|---|---|---|
| $A$ ($\times 10^{-1}$) | 4.98 | 1.53 | 5.68 |
| $B$ ($\times 10^{-3}$) | 5.59 | 1.62 | 11.55 |
| $C$ ($\times 10^{-5}$) | 1.45 | 0.61 | 2.77 |
| $D$ ($\times 10^{-1}$) | 7.34 | 2.35 | 7.89 |
| $E$ ($\times 10^{-3}$) | 2.96 | 1.34 | 11.24 |
| $F$ ($\times 10^{-7}$) | 8.35 | 3.74 | 10.00 |
| $n$ | 3.20 | 2.85 | 3.20 |
| $m$ | 4.16 | 4.07 | 4.45 |
| $a$ | 0.94 | 0.57 | 1.07 |
| $b$ | 1.01 | 0.97 | 1.03 |
| $\alpha$ | 1.32 | 0.77 | 10.06 |